Solid Freeform Fabrication 2017: Proceedings of the 28th Annual International Solid Freeform Fabrication Symposium – An Additive Manufacturing Conference
Reviewed Paper

COMPETING INFLUENCE OF POROSITY AND MICROSTRUCTURE ON THE FATIGUE PROPERTY OF LASER POWDER BED FUSION STAINLESS STEEL 316L

Meng Zhang[1], Chen-Nan Sun[2], Xiang Zhang[3], Phoi Chin Goh[4], Jun Wei[2], Hua Li[1*], David Hardacre[4]

[1] Singapore Centre for 3D Printing, School of Mechanical and Aerospace Engineering, Nanyang Technological University, 50 Nanyang Avenue, Singapore 639798
[2] Singapore Institute of Manufacturing Technology, A*STAR, 73 Nanyang Drive, Singapore 637662
[3] Faculty of Engineering & Computing, Coventry University, Coventry CV1 5FB, UK
[4] Lloyd's Register Global Technology Centre, 1 Fusionopolis Place, #09-11 Galaxis, Singapore 13852
*Corresponding author: lihua@ntu.edu.sg

Abstract

Crack initiation constitutes a large portion of the total life for parts under high cycle fatigue loading. Materials made by the laser powder bed fusion (L-PBF) process contain unavoidable process-induced porosity whose effect on the mechanical properties needs to be considered for fatigue applications. Results from this work show that not all pores in L-PBF parts promote fatigue crack initiation. The length scale of local microstructure defects, i.e. grain boundary, could be larger than the pores and in such cases they are the primary cause for crack initiation. Samples were produced in this work to demonstrate the critical defect size responsible for the transition between the porosity-driven and microstructure-driven failure modes.

Keywords: Fatigue; porosity; microstructure; powder bed fusion; selective laser melting; stainless steel 316L

1. Introduction

Additive manufacturing (AM) is a family of advanced manufacturing methods which produces near net-shape parts with complex geometry based on input from computer-aided design. Its forming principle is different from conventional subtractive manufacturing methods, as objects are built in a layerwise manner. Thus, while offering substantial design freedom and more efficient utilization of resources, different mechanical properties and applications are expected of parts built by AM processes. Laser powder bed fusion (L-PBF) is a popular metal AM process which uses high power laser as the energy source to melt powdered raw material. It has been widely explored as the means of manufacturing for the aerospace, automotive and medical industries for producing lightweight and novel structures.

Stainless steel 316L is an extra-low carbon austenitic chromium-nickel stainless steel which has shown good compatibility with the L-PBF process. It is frequently used for its good corrosion resistance, particularly in biomedical and marine-related applications. Fully dense stainless steel 316L parts with superior strength to that of the conventional manufacturing processes and good ductility have been produced [1]. However, concerns regarding the fatigue behaviour of L-PBF parts had been raised as process-induced porosities were shown to cause

fatigue crack initiation and premature failure [2-7]. As the applications of stainless steel 316L often desire good fatigue resistance, such as in the case of orthopaedic implants, the influence of L-PBF process parameters and the resulting porosity level on this particular aspect of mechanical property requires some due attention.

It is known that fatigue failure occurs as a result of the competition between microstructure and voids in polycrystalline materials [8, 9]. Conventional manufacturing processes, such as casting and welding, produce parts containing microcavities and shrinkage defects. For L-PBF, the localized heating and rapid cooling, coupled with the use of powder as the feedstock, can lead to the formation of defects, such as lack of fusion and gas pores. The choice of process parameter settings, such as layer thickness, laser power, scan strategy and hatch, strongly influence the shape, size and number of the defects [10]. In comparison with a number of alloys such as Ti6Al4V, Inconel 718 and carbon steel, stainless steel 316L was shown to be one of the alloys with the highest susceptibility to forming lack of fusion defects [11]. This is possibly a results of its high thermal conductivity, which reduces its ability at retaining heat [12]. Any process inconsistency, e.g. uneven powder layers being deposited due to damaged recoater and process parameter deviations from the preset values, may subject stainless steel 316L to defect formation even under optimized processing conditions. This implies that stainless steel 316L components produced by L-PBF could be prone to defect-induced failure under cyclic loading.

When acceptable control of defect size is achieved, e.g. by the choice of appropriate processing parameter, such that the defects are small in comparison to the local microstructure heterogeneities, they may be considered as benign. Conventionally, non-metallic inclusions smaller than 5 μm are usually harmless for low purity parts [13]. Precise determination of the critical pore size is difficult due to the random arrangement of local microstructure. For example, the non-propagating crack size of a 0.13% C steel was found to be in the order of 100 μm, even though the average grain size was only 34 μm [14]. For L-PBF stainless steel 316L, studies on this aspect of the fatigue behaviour is not available. In terms of the influence of microstructure on fatigue property, a number of studies had highlighted the importance of grain size and texture on fatigue crack initiation and growth. Leuders *et al*. [15] and Riemer *et al*. [16] tested the effect of stress relieving heat treatment and hot isostatic pressing on the high cycle fatigue and crack growth behaviour of stainless steel 316L respectively. Both concluded that residual stress and porosity have insignificant impact on the fatigue resistance and attributed such behaviour to its high ductility. As the austenitic structure of stainless steel 316L does not undergo phase transformation during cooling, it does not contain the martensite phase and therefore brittle failure is avoided. This could have led to the high ductility and defect-tolerant behaviour [16]. Another source of microstructure defects in L-PBF parts is the melt pool boundary. It was found to impact failure under monotonic tensile loading and give rise to anisotropic properties [17]. Anisotropic fatigue behaviour had also been observed in L-PBF-processed stainless steel 316L parts, where the vertically-built specimens produced shorter fatigue life [3, 18]. The competing influence of grain, porosity and melt pool boundary could be responsible for such behaviour and this needs to be addressed in detail.

As existing studies did not provide explicit information on the density and porosity conditions of their samples, quantitative correlations between porosity, microstructure and fatigue properties cannot be made from the previous works. Considering that there is a lack of international standards for the certification and quality assurance of part made by powder bed

fusion, a systematic examination of the process-structure-property relationship for L-PBF is desirable for the adoption of this process for structural applications. In view of this gap, this study aims to provide qualitative and quantitative evaluation of the competing influence of porosity and microstructure on the high cycle fatigue properties of L-PBF stainless steel 316L. Experimental and analytical results from this work can be used as a preliminary guide on the possible failure modes for L-PBF parts with different porosity conditions.

2. Experimental Setup

Commercially available stainless steel 316L powder with spherical shape and mean diameter of 17 μm was used. Four sets of samples were fabricated by the EOS M 290 system at layer thickness settings of 20 μm, 40 μm, 60 μm and 80 μm, while keeping all the other process parameters, such as laser power, scan speed and hatch, constant; they are referred to as T1, T2, T3 and T4 respectively in this work. Rectangular blocks were built with the long edge being oriented at an angle from the recoating direction, as shown in Figure 1(a), to prevent uneven powder deposition due to the interaction between the part and the recoater blade [19]. After being removed from the baseplate, the blocks were subsequently machined to produce the samples for mechanical testing. Small test blocks were built adjacent to them for porosity characterization and metallographic examination.

Density of the test blocks was measured by the Archimedes method (Mettler Toledo XS204) and micrograph analysis of planes parallel to the build direction. Since fatigue failure is sensitive to the largest occurring defects, inspection was also performed to estimate the size distribution of the large defects. This was done by taking 30 random images of areas $0.31\ mm^2$ each using optical microscope and identifying the largest defect size within each image [20, 21]. The equivalent spherical pore diameters were then calculated and used as the input for fitting the Gumbel Extreme Value Distribution, following the maximum likelihood method as described in the ASTM E2283. The cumulative distribution is given by

$$F(x) = \exp(-\exp\left(-\frac{x-\lambda}{\delta}\right)) \quad (1)$$

where x is the equivalent spherical pore diameter, λ and δ are the location and scale parameters of the Gumbel distribution respectively.

Fatigue test samples were designed in accordance to ASTM E466 (Figure 1 (b)). They were machined from the rectangular blocks in Figure 1 (a) by the wire cut electrical discharge machining (EDM) method, followed by manual grinding to remove the resulting surface layers. Samples were extracted from each block along the z-axis such that the loading direction was perpendicular to the build direction. Fatigue tests were conducted in air under a constant force-controlled sinusoidal loading at R=0.1 on a servo hydraulic testing system (MTS 810) at a frequency of 5 Hz.

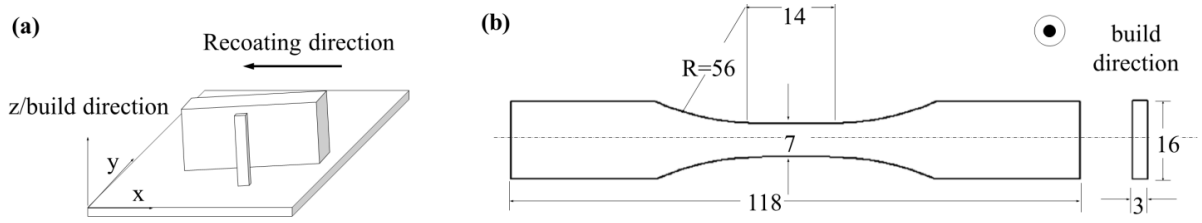

Figure 1 (a) Rectangular blocks and small test blocks were built at an angle from the recoating direction, (b) geometry of fatigue test samples (dimensions in mm). Eight samples were extracted from each rectangular block along the z-axis by wire cutting.

3. Results

3.1 Porosity – Volume Fraction and Size Distribution

Optical micrographs in Figure 2 (a)-(d) show the porosity on the vertical planes of the test blocks. T1 and T2 contain predominantly small spherical pores. For T3, there is a sudden increase in the pore size and the pores are irregular in shape. This indicates that sufficient remelting of the previously deposited powder layer can no longer be achieved at this layer thickness, resulting in the formation of lack of fusion defects. Further increase in layer thickness at T4 led to a large increase in the number of lack of fusion defects, such that they were in closer proximity to each other. This observation is consistent with the measured relative densities shown in Table 1, except that the Archimedes method is unable to capture the small change in porosity between T1 and T2.

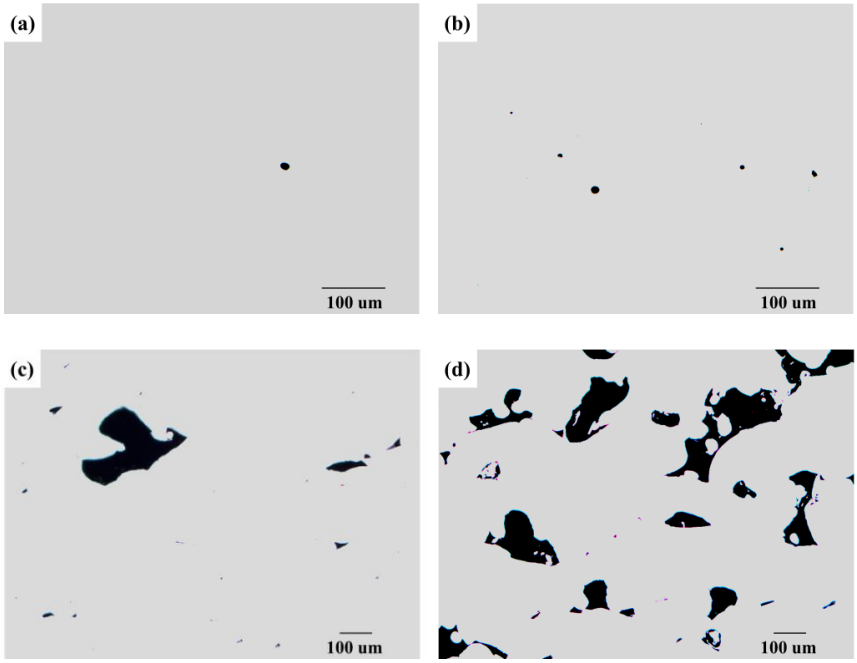

Figure 2 (a) – (d) Optical micrographs showing porosity (in black) on planes parallel to the build direction for T1, T2, T3 and T4 respectively.

The Gumbel distribution parameters of the samples are also shown in Table 1. The value of λ is equal to the mode of the Gumbel distribution, i.e. the equivalent spherical pore diameter with the highest frequency of occurrence in a sample. For near fully dense parts, i.e. T1 and T2, most of the pores are in the order of 10 μm. At close to 99% relative density (based on the image analysis method), i.e. T3, large pores in the order of 50 μm are already present. Also, in addition to the increase in pore size, the pores are more widely distributed with increasing layer thickness, as shown by the values of the scale parameter δ. This is mainly due to stereological effect where cutting sample for metallographic examination exposed the irregularly-shaped defects at different sections along their length. In fact, for T3 and T4, the assumption of spherical defects in estimating the pore size is no longer valid. The orientation of the pores with respect to the loading direction is important for estimating the size of these defects. However, for simplicity, spherical defects were assumed in this work. Lastly, in comparison with the Archimedes method, the Extreme Value Distribution was able to capture the small increase in pore size from T1 to T2, as indicated by the larger λ value.

Table 1 Density of the samples measured by the Archimedes method and image analysis of the optical micrographs, and the Gumbel Extreme Value Distribution parameters for describing the equivalent spherical pore diameter distributions of the largest-occurring defects.

Sample ID	Layer thickness (μm)	Relative density (%)		Gumbel distribution parameter	
		Archimedes	Image analysis	Location parameter λ(μm)	Scale parameter δ(μm)
T1	20	98.93±0.08	99.98±0.05	6.6	4.3
T2	40	99.14±0.01	99.92±0.18	13.4	7.6
T3	60	98.11±0.02	98.88±0.95	53.6	35.9
T4	80	91.95±0.14	93.66±3.15	146.6	51.7

3.2 High Cycle Fatigue and Facture Behaviour

Fatigue Life

Figure 3 shows the fatigue life of the samples. T1 and T2 are nearly identical. Using T1 as the reference, the fatigue lives of T3 and T4 were reduced significantly, by 65% and 94% respectively. The change in fatigue resistance is proportional to the relative densities of the samples, indicating that porosity plays an important role on the failure of T3 and T4 relative to T1 and T2.

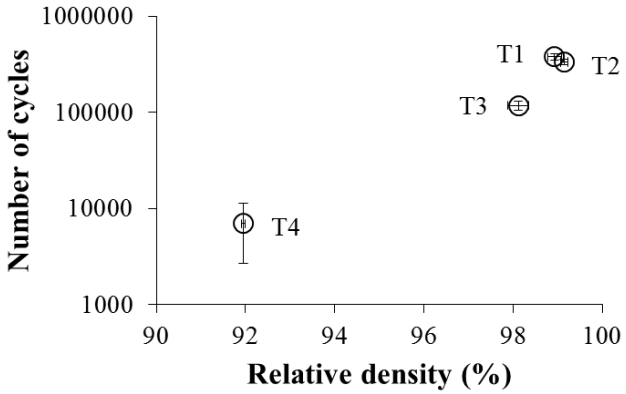

Figure 3 Fatigue life of laser powder bed fusion stainless steel 316L samples subjected to maximum cyclic loading of 438 MPa.

Fractography

Figure 4 displays the SEM images of the fracture surfaces after fatigue tests. The dotted lines in Figure 4 (a) and (c) separate the fatigue crack origins from the crack propagation region for T1 and T2 respectively. Figure 4 (b) and (d) are the enlarged views of the crack initiation regions. Both samples exhibited intergranular crack initiation behaviour. The arrows in Figure 4 (b) and (c) indicate intergranular de-bonding at grain boundaries. Comparing the two samples, T2 contained a larger crack initiation region with more extensive intergranular cracking. Figure 4 (d) shows a large area of neatly arranged dendritic cells. The presence of intergranular fracturing and micro-cracks is explained as follows: during solidification, the rapid cooling process could have resulted in competitive grain growth at the solid-liquid interface and caused the formation of differently oriented grains at the melt pool [22] and a large amount of dislocations, even though the global grain orientation is parallel to the build direction, i.e. epitaxial grain. Material deformation by the slip mechanism is constrained by the grain boundaries, where dislocation pile-up can trigger intergranular fatigue cracking [23]. Increasing the layer thickness could have led to less extensive remelting and grain regrowth. Grain boundary defects were thus more prevalent for T2 than T1, contributing to the larger crack initiation region.

SEM image of the fracture surface of T3 in Figure 4 (e) shows fatigue crack initiation from a surface defect in the order of 100 μm. This is comparable with the defect size obtained from the Extreme Value Distribution. Materials transited rapidly into the propagation mode once cracks were initiated. Cracks could have been initiated at many other lack of fusion defects in the material subsurface. They joined the main crack propagation path and became visible on the fracture surface. Overall, these lack of fusion defects had resulted in the near 60% reduction in fatigue life for T3 as compared to T1. For T4, the influence of porosity on fatigue failure became even more significant. No distinct crack origin could be identified in Figure 4 (f). The large amount of defects significantly reduced the load-bearing capacity of the material. The interaction of closely spaced pores compounded the effect by increasing the local stress concentration and multiple cracks were initiated simultaneously, leading to the much lower fatigue strength.

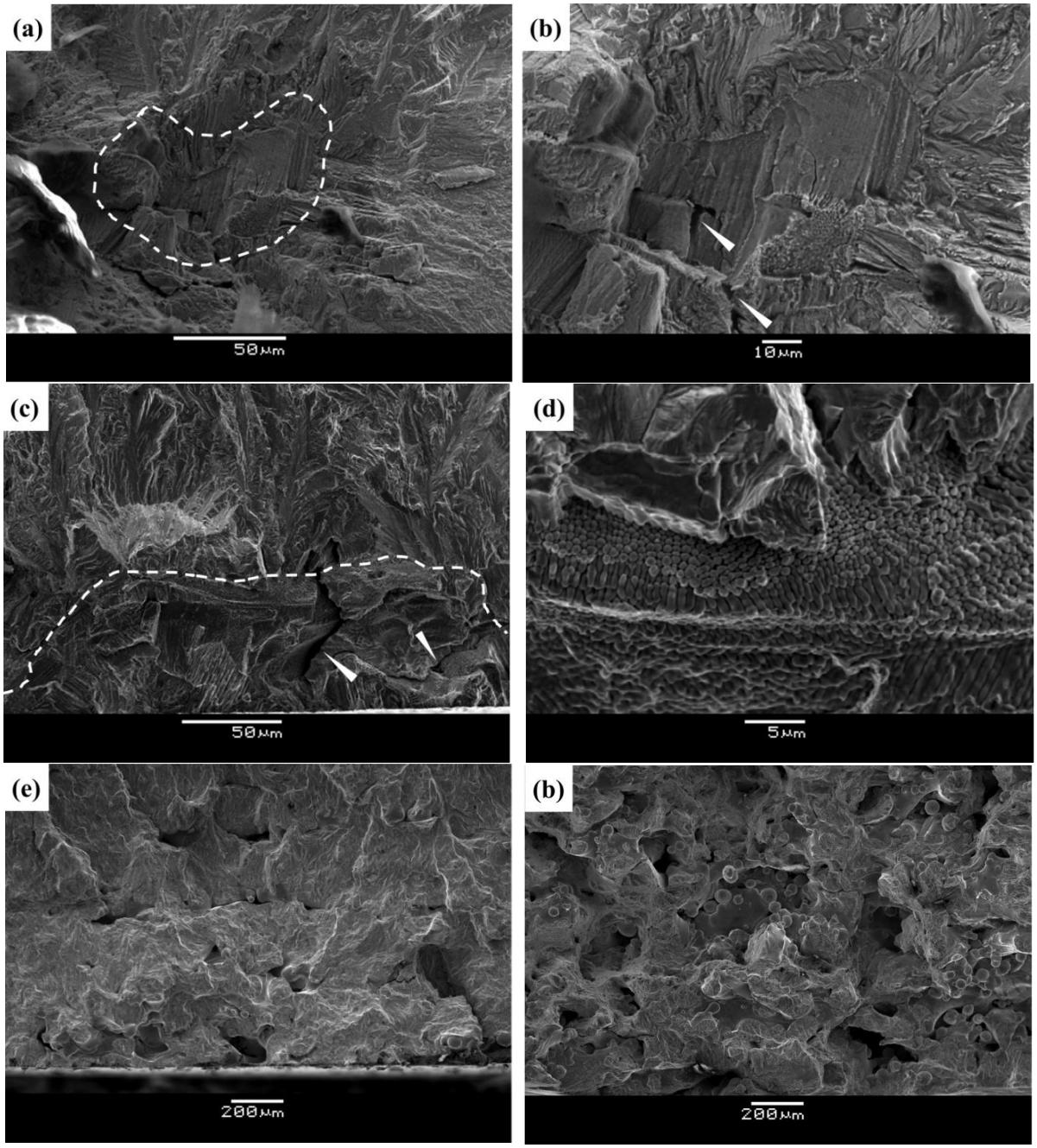

Figure 4 SEM images of sample fracture surfaces. (a) T1 showing transition from mixed intergranular and transgranular fracture at the crack initiation site (within dotted line) to transgranular propagation, (b) enlarged view of (a) showing debonding at sub-grain boundaries (white arrows), (c) T2 showing a larger and more intergranular crack initiation region than T1, (d) enlarged view of (c) showing sub-grains revealed by intergranular fracture, (e) T3 showing crack initiation from lack of fusion defect at the sample surface, and (f) T4 showing extensive lack of fusion defects and no discernible major crack origin.

4. Discussions – Competition between Microstructure and Porosity

Based on the experimental fatigue test results, it appears that the failure mechanism of T1 and T2 is different from T3 and T4. Specifically, fatigue crack initiation in T1 and T2 was predominantly driven by grain boundary defects, while T3 and T4 failed due to crack initiation at porosity. This section provides the discussions on the effect of microstructure and porosity on the observed properties.

4.1 Fatigue Limit

For low cyclic stress conditions, the size of the local plastic zone is in the order of short range microstructure and the influence of local microstructural heterogeneity is very significant [24]. Consequently, the growth of small and large fatigue cracks are fundamentally different at applied cyclic stress close to the fatigue limit. The Kitagawa-Takahashi concept had been used for defining the critical defect size a_0 below which fatigue strength is not affected by changes in crack size [9]. Based on the work by Kitagawa and Takahashi [25], the relationship between crack length a and the stress range for crack propagation ΔS can be described by the equation derived by El Haddad *et al*. [26]:

$$\Delta S = \frac{\Delta K_{\text{th}}}{F\sqrt{\pi(a+a_0)}} \tag{2}$$

where ΔK_{th} is the threshold stress intensity factor range, F is a geometric factor and a is the crack size. For a defect-free component with fatigue limit ΔS_{e}, a_0 is a material constant described by:

$$a_0 = \left(\frac{\Delta K_{\text{th}}}{F\Delta S_{\text{e}}}\right)^2 \frac{1}{\pi} \tag{3}$$

A planar near surface circular defect was modelled to evaluate the influence of defect size on the fatigue crack propagation stress, i.e. the fatigue limit. Experimentally determined fatigue crack growth data [16] and the BS7910 [27] for calculating F were used. Figure 5 shows the Kitagawa-Takahashi diagram in terms of Equation (2) and the fatigue limit results obtained in this work. Since λ is equal to the mode of the Gumbel distribution, its values, as presented in Table 1, are representative of the equivalent spherical pore diameters of the samples and were used for estimating the crack size a. As two cracks could be considered as originating from the two ends of the planar defect, the crack size $a = \lambda/2$. It can be seen from Figure 5 that cracks originating from process-induced pores for T1 and T2 are in the short fatigue crack regime where fatigue limits are not influenced by the crack size. This agrees with results from the fractography analysis, where pores in T1 and T2 were too small that cracks originated at the grain boundary defects instead. Porosity-induced cracks in T3 and T4 are approaching the transition region between short and long fatigue cracks. For T4, the model considerably over-estimates the fatigue limit; this is because rather than containing an isolated pore, as assumed by the model, sub-optimal processing in L-PBF produces parts with homogenously distributed defects. Neighbouring pores were in close proximity to each other and imposed greater stress concentration, resulting in the lower fatigue strength. Also, the assumption of spherical defects in deriving λ could have underestimated the actual pore size of T3 and T4, where irregular pores were prevalent. An appropriate factor on strength needs to be applied to account for these effects. In summary, process-induced pores in T1 and T2 were in the short fatigue crack regime and were too small to cause crack initiation. Crack initiation from grain boundary led to the similar fatigue

limits of these samples. For T3 and T4, process-induced pores were large enough to cause fatigue crack initiation, leading to the crack size-dependent fatigue limits.

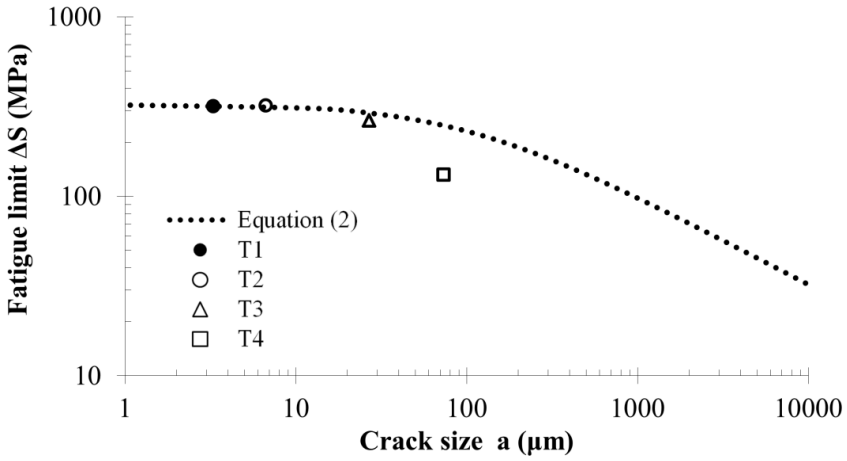

Figure 5 Kitagawa-Takahashi diagram comparing the El Haddad model and the experimental high cycle fatigue test data from this work.

4.2 Critical Defect Size

It is of practical interest to define the critical pore size for ensuring the reliability of components under high cycle fatigue loading. The Kitagawa-Takahashi analysis can only be used to provide theoretical but not accurate estimate of the critical pore size. Experimental results from this work shows that this transition exists between the pore size of T2 and T3, such that 13.4 μm $< \lambda_{critical} <$ 53.6 μm. This should be interpreted in conjunction with the size of the local microstructure. Figure 7 shows the microstructure on the plane parallel to the build direction for a typical L-PBF stainless steel 316L. As observed from the fractographs, intergranular failure could have occurred at the boundary between differently oriented grains. The lengths at such grain boundaries are marked in Figure 6. They are mostly in the order of 30 μm to 40 μm. Since the pores in T2 are smaller, microstructure boundaries become the detrimental defects. For T3, the pores are larger than the size of the local microstructure and they become the most critical defects that trigger fatigue cracking. However, it is to be noted that while results from this work provided evidence to the critical defect size in L-PBF stainless steel 316L, they may be limited to the processing parameter region (optimised for a layer thickness of 20 μm) and scan strategy used in this work, as changing the process settings could lead to different microstructure length scales.

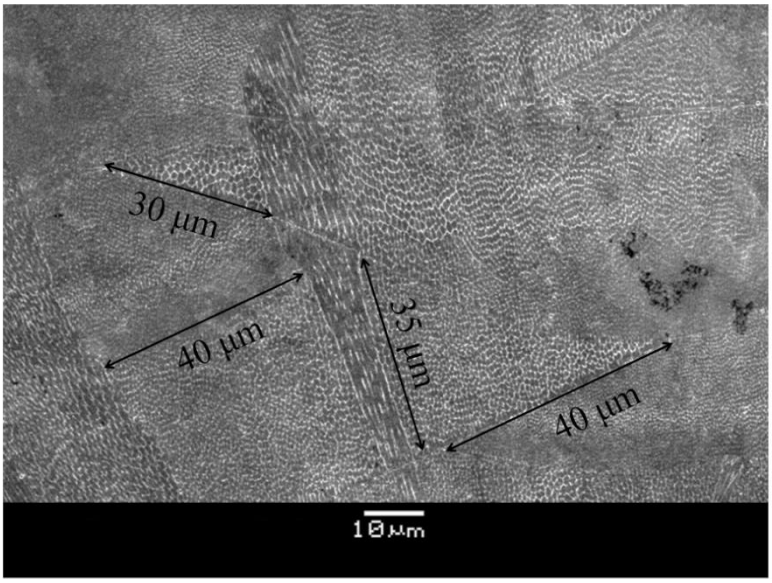

Figure 6 SEM image showing characteristic microstructures of L-PBF parts. The lengths of the boundaries between some different oriented grains are shown.

5. Conclusions

The following conclusions were drawn from the results obtained in this work:

1) Two fatigue failure modes are possible for stainless steel 316L manufactured by the L-PBF process depending on the level of porosity. For parts containing small pores, grain boundary defect-driven crack initiation is the predominant failure mode (T1 and T2). Parts containing large pores are prone to porosity-driven crack initiation (T3 and T4), which significantly reduced the high cycle fatigue life. When pores are too large and close to each other (T4), local stress concentration increases due to interaction among the pores, resulting in much greater reduction in fatigue strength.

2) Having established that the transition in fatigue crack initiation modes occurred between T2 and T3, their porosity parameters were compared with the size of the local microstructure heterogeneity. The pore size and volume fraction of T2 could be used as a conservative estimate of the critical pore size that triggers porosity-induced fatigue crack initiation.

References

[1] I. Tolosa, F. Garciandía, F. Zubiri, F. Zapirain, A. Esnaola, Study of mechanical properties of AISI 316 stainless steel processed by "selective laser melting", following different manufacturing strategies, Int. J. Adv. Manuf. Technol. 51(5-8) (2010) 639-647.
[2] A. Yadollahi, N. Shamsaei, S.M. Thompson, A. Elwany, L. Bian, Effects of building orientation and heat treatment on fatigue behavior of selective laser melted 17-4 PH stainless steel, Int. J. Fatigue 94 (2017) 218-235.

[3] R. Shrestha, J. Simsiriwong, N. Shamsaei, S.M. Thompson, L. Bian, Effect of build orientation on the fatigue behavior of stainless steel 316l manufactured via a laser-powder bed fusion process.
[4] E. Brandl, U. Heckenberger, V. Holzinger, D. Buchbinder, Additive manufactured AlSi10Mg samples using Selective Laser Melting (SLM): Microstructure, high cycle fatigue, and fracture behavior, Mater. Des. 34 (2012) 159-169.
[5] S. Leuders, M. Thöne, A. Riemer, T. Niendorf, T. Tröster, H.A. Richard, H.J. Maier, On the mechanical behaviour of titanium alloy TiAl6V4 manufactured by selective laser melting: Fatigue resistance and crack growth performance, Int. J. Fatigue 48 (2013) 300-307.
[6] M. Akita, Y. Uematsu, T. Kakiuchi, M. Nakajima, R. Kawaguchi, Defect-dominated fatigue behavior in type 630 stainless steel fabricated by selective laser melting, Mater. Sci. Eng., A 666 (2016) 19-26.
[7] H. Gong, K. Rafi, T. Starr, B. Stucker, Effect of defects on fatigue tests of as-built Ti-6Al-4V parts fabricated by selective laser melting, Solid freeform fabrication symposium, University of Texas Austin, Texas, 2012, pp. 499-506.
[8] R. Guerchais, F. Morel, N. Saintier, C. Robert, Influence of the microstructure and voids on the high-cycle fatigue strength of 316L stainless steel under multiaxial loading, Fatigue Fract. Eng. Mater. Struct. 38(9) (2015) 1087-1104.
[9] F. Morel, R. Guerchais, N. Saintier, Competition between microstructure and defect in multiaxial high cycle fatigue, Frattura ed Integrità Strutturale (33) (2015) 404.
[10] G. Kasperovich, J. Haubrich, J. Gussone, G. Requena, Correlation between porosity and processing parameters in TiAl6V4 produced by selective laser melting, Mater. Des. 105 (2016) 160-170.
[11] T. Mukherjee, J. Zuback, A. De, T. DebRoy, Printability of alloys for additive manufacturing, Scientific reports 6 (2016).
[12] A. Mertens, S. Reginster, H. Paydas, Q. Contrepois, T. Dormal, O. Lemaire, J. Lecomte-Beckers, Mechanical properties of alloy Ti–6Al–4V and of stainless steel 316L processed by selective laser melting: influence of out-of-equilibrium microstructures, Powder Metall. 57(3) (2014) 184-189.
[13] U. Krupp, Fatigue crack propagation in metals and alloys: microstructural aspects and modelling concepts, John Wiley & Sons2007.
[14] Y. Murakami, Metal fatigue: effects of small defects and nonmetallic inclusions, Elsevier2002.
[15] S. Leuders, T. Lieneke, S. Lammers, T. Tröster, T. Niendorf, On the fatigue properties of metals manufactured by selective laser melting–The role of ductility, J. Mater. Res. 29(17) (2014) 1911-1919.
[16] A. Riemer, S. Leuders, M. Thöne, H. Richard, T. Tröster, T. Niendorf, On the fatigue crack growth behavior in 316L stainless steel manufactured by selective laser melting, Eng. Fract. Mech. 120 (2014) 15-25.
[17] W. Shifeng, L. Shuai, W. Qingsong, C. Yan, Z. Sheng, S. Yusheng, Effect of molten pool boundaries on the mechanical properties of selective laser melting parts, J. Mater. Process. Technol. 214(11) (2014) 2660-2667.
[18] T.M. Mower, M.J. Long, Mechanical behavior of additive manufactured, powder-bed laser-fused materials, Mater. Sci. Eng., A 651 (2016) 198-213.
[19] P.J. da Silva Bartolo, A.C.S. de Lemos, A.M.H. Pereira, A.J.D.S. Mateus, C. Ramos, C. Dos Santos, D. Oliveira, E. Pinto, F. Craveiro, H.M.C. da Rocha Terreiro, High Value Manufacturing: Advanced Research in Virtual and Rapid Prototyping: Proceedings of the 6th International

Conference on Advanced Research in Virtual and Rapid Prototyping, Leiria, Portugal, 1-5 October, 2013, CRC Press2013.
[20] Y. Murakami, S. Beretta, Small defects and inhomogeneities in fatigue strength: experiments, models and statistical implications, Extremes 2(2) (1999) 123-147.
[21] S. Beretta, Y. Murakami, Statistical analysis of defects for fatigue strength prediction and quality control of materials, Fatigue Fract. Eng. Mater. Struct. 21(9) (1998) 1049-1065.
[22] D. Wang, C. Song, Y. Yang, Y. Bai, Investigation of crystal growth mechanism during selective laser melting and mechanical property characterization of 316L stainless steel parts, Mater. Des. 100 (2016) 291-299.
[23] Z. Zhang, Z. Wang, Dependence of intergranular fatigue cracking on the interactions of persistent slip bands with grain boundaries, Acta Mater. 51(2) (2003) 347-364.
[24] A. Pineau, S.D. Antolovich, Probabilistic approaches to fatigue with special emphasis on initiation from inclusions, Int. J. Fatigue 93 (2016) 422-434.
[25] H. Kitagawa, S. Takahashi, Applicability of fracture mechanics to very small cracks or the cracks in the early stage, Second International Conference on Mechanical Behavior of Materials. ASM, Metals Park, Ohio. 1976, 627-631, 1976.
[26] M. El Haddad, T. Topper, K. Smith, Prediction of non propagating cracks, Eng. Fract. Mech. 11(3) (1979) 573-584.
[27] BS 7910 Guide to methods for assessing the acceptability of flaws in metallic structures, 2013.